RESEARCH ARTICLE

Fabrication of magnetic $Fe_3O_4@SiO_2@Bi_2O_2CO_3$/rGO composite for enhancing its photocatalytic performance for organic dyes and recyclability

Gang Su[1] · Lihua Liu[1,2,3] (ID) · Lixing Zhang[1] · Xing Liu[1] · Jianrong Xue[1,2,3] · Anping Tang[1,2,3]

Abstract

A novel magnetic $Fe_3O_4@SiO_2@Bi_2O_2CO_3$/rGO composite comprising of uniform core-shell-structured $Fe_3O_4@SiO_2@Bi_2O_2CO_3$ microspheres mounted on reduced graphene oxide (rGO) sheets was successfully fabricated by using a facile hydrothermal method. The adsorption–desorption isotherm of $Fe_3O_4@SiO_2@Bi_2O_2CO_3$/rGO belonged to type IV with an H4-type hysteresis loop. The specific surface areas and magnetization saturation value (M_s) of $Fe_3O_4@SiO_2@Bi_2O_2CO_3$/rGO ($x = 0.15$ g) were 102.12 m^2/g and 25.4 emu/g, respectively. $Fe_3O_4@SiO_2@Bi_2O_2CO_3$/rGO ($x = 0.15$ g) exhibited remarkable photocatalytic degradation activity and mineralization effect for MO and decolorization performance for the mixed solution of MO, Rh B, and MB. MO degradation by $Fe_3O_4@SiO_2@Bi_2O_2CO_3$/rGO conformed to a first-order kinetic reaction, and the corresponding k_{app} value was 0.05553 min^{-1}. A suitable amount of rGO in $Fe_3O_4@SiO_2@Bi_2O_2CO_3$/rGO could decrease the energy band gap, inhibit the recombination of photo-induced electron/hole (e^-/h^+) pair, and broaden and enhance the response of the catalyst to visible light, thereby enhancing the visible-light catalytic degradation of organic dyes. The active species produced in the photocatalysis included $\cdot O_2^-$, $\cdot OH$, and h^+, with $\cdot O_2^-$ being the dominant active species. The as-prepared photocatalyst also showed excellent magnetic separation performance and stability. Results show that the as-prepared $Fe_3O_4@SiO_2@Bi_2O_2CO_3$/rGO composite is a promising photocatalyst with considerable application potential in organic dyes removal.

Keywords Degradation mechanism · Hydrothermal synthesis · Magnetic $Fe_3O_4@SiO_2@Bi_2O_2CO_3$/rGO composite · Organic dye · Visible-light photocatalytic degradation

Introduction

Methyl orange (MO), rhodamine B (Rh B), and methylene blue (MB) are typical organic dyes that are widely used in industrial products and laboratory research (Jiang et al. 2017; Minitha et al. 2017) and have become one of the largest groups of contaminants in many wastewaters. Given their complex aromatic structure, difficult degradation, and strong toxicity, dye wastewater can cause serious environmental pollution and pose a potential threat to human health. Several

✉ Lihua Liu
llh213@163.com

Gang Su
875042174@qq.com

Lixing Zhang
460259515@qq.com

Xing Liu
1249158985@qq.com

Jianrong Xue
xjr_1111@163.com

Anping Tang
anpingxt@126.com

[1] School of Chemistry and Chemical Engineering, Hunan University of Science and Technology, Xiangtan 411201, China

[2] Key Laboratory of Theoretical Organic Chemistry and Function Molecule, Ministry of Education, Xiangtan 411201, China

[3] Hunan Provincial Key Laboratory of Controllable Preparation and Functional Application of Fine Polymers, Xiangtan 411201, China

techniques, such as adsorption, reverse osmosis, biological degradation, chemical and advanced oxidation method, and photocatalytic degradation, have been extensively studied for their application in removing these contaminants. Photodegradation based on semiconductor materials is considered one of the most effective approaches for contaminant removal due to its deep oxidation, ease of operation (Zhang et al. 2019a), and utilization of natural or artificial illumination (Guo et al. 2016). However, this method often encounters problems related to its poor morphology, band gap width, high photo-induced electron/hole (e^-/h^+) pair recombination rate, and difficult recovery. These problems have been associated with the low light-absorption rate, poor quantum and photodegradation efficiency, and cumbersome operation of this method. Quite a few photocatalysts, such as TiO_2 and ZnO, can exhibit photocatalytic activity only by ultraviolet (UV; $\lambda \leq 387.5$ nm) irradiation due to their excessive band gap widths (ZnO and TiO_2 3.2 eV) (Ling et al. 2019). By contrast, the UV radiation content of solar radiation accounts for only 5% of the total solar radiation illumination (Anwer et al. 2019). Therefore, new visible-light-driven photocatalytic materials must be designed and developed based on an effective utilization of solar energy.

Among many visible-light catalysts, bismuth semiconductors, such as $BiFeO_3$ (Wu et al. 2019), $BiVO_4$ (Omrani and Nezamzadeh-Ejhieh 2020), Bi_2WO_6 (Zang et al. 2019), Bi_2MoO_6 (Varma et al. 2020), BiOX (Marcelino and Amorim 2019), and $Bi_2O_2CO_3$ (Deng et al. 2020), have attracted wide attention due to their unique layered structure and excellent photocatalytic properties. As a typical Aurivillius-type oxide, $Bi_2O_2CO_3$ belongs to the tetragonal system and has a unique layered structure comprising of alternating layers of $[Bi_2O_2]^{2+}$ and CO_3^{2-}. The internal electric field generated by polarization is conducive to the separation of photo-induced electrons and holes, which can improve the photocatalytic performance of $Bi_2O_2CO_3$ (Zhang et al. 2016). However, the large band gap value of $Bi_2O_2CO_3$ (3.2 eV–3.5 eV) (Fan et al. 2019) implies a high photogenic carrier recombination rate (Peng et al. 2013) and low quantum efficiency, further highlighting the need to improve photocatalytic activity. An excellent and practical photocatalyst should possess not only a high specific surface area to induce redox reactions and a minimizing recombination to generate a photo-induced charge but also an excellent separation and recycling performance after wastewater treatment. Various strategies, including heteroatom doping (Li et al. 2018), composition techniques (Bian et al. 2018), heterojunction configuration (Ran et al. 2020), surface decoration and control of morphology (Zhao et al. 2019), and microstructuring approaches (Su and Wu 2018), have been adopted to improve the essential properties of $Bi_2O_2CO_3$. Graphene/reduced graphene oxide (G/rGO) can promote the transfer of photo-induced electrons and reduce the recombination probability of photo-induced carriers in semiconductors (Liu et al.

2019a) owing to their typically conjugated large π bond structure, zero band gap energy, large specific surface area, and high electron mobility (Jiang et al. 2019). Therefore, G/rGO has been used to improve the photocatalytic activity of photocatalysts, such as the graphene/$Bi_2O_2CO_3$ composite catalyst (Li et al. 2020), core–shell structure of $Bi_2O_2CO_3$@rGO (Gurusamy et al. 2017), and $Bi_2O_2CO_3$ flower-shaped heterogeneous junction modified by graphene and TiO_2 (Ao et al. 2015). However, the abovementioned photocatalysts are prepared with sodium citrate, urea, or PVP templates by means of a two-step method at a high temperature for a long time, thereby resulting in their complex preparation, difficult structure control, and high cost. In addition, photocatalysts cannot be conveniently separated from wastewater and have poor recycling performance, thereby restricting their application in actual wastewater treatment. Many studies have proven that compositing prepared materials with Fe_3O_4 particles to endow composite magnetic properties is feasible if the external magnetic field is considered (Li et al. 2016b). However, the direct combination of photocatalysts with Fe_3O_4 cores may accelerate the recombination of e^-/h^+ pairs due to the heterojunction between Fe_3O_4 and the photocatalyst, thereby reducing photocatalytic efficiency (Su et al. 2021). Furthermore, Fe_3O_4 is unstable under acidic conditions (Do et al. 2018) and has poor oxidation resistance. Coating a layer of SiO_2 on Fe_3O_4 microspheres to form a core–shell architecture has been proven effective in addressing such issues (Wang et al. 2016; Teixeira et al. 2017).

In this study, a novel Fe_3O_4@SiO_2@$Bi_2O_2CO_3$/rGO composite with an excellent visible photocatalytic degradation performance for organic dyes and an outstanding magnetic separability was designed and controllably fabricated by using a facile green hydrothermal method with Fe_3O_4@SiO_2 microspheres as a core, porous $Bi_2O_2CO_3$ as an active layer, and rGO as a modifying agent. The microstructure, morphology, and related physicochemical properties of the as-obtained Fe_3O_4@SiO_2@$Bi_2O_2CO_3$/rGO composite were measured systematically. The visible photocatalytic performances of Fe_3O_4@SiO_2@$Bi_2O_2CO_3$/rGO were evaluated by the photodegradation of MO, Rh B, and MB, and the related degradation mechanism was explored by using the diffuse reflectance UV–visible spectrum (UV–vis DRS), photoluminescence spectrum (PL), electrochemical impedance spectrum (EIS), and free radical capture test. To the best of our knowledge, no previous report has attempted to comprehensively discuss the preparation and evaluation of the visible photocatalytic degradation performance of Fe_3O_4@SiO_2@$Bi_2O_2CO_3$/rGO for organic dyes in wastewater. Results show that the proposed magnetic composite not only has the high specific surface area and porous surfaces of $Bi_2O_2CO_3$ but also has excellent visible photocatalytic degradation properties, easy separability, and recyclability from wastewater. The well-designed visible photocatalyst offers broad application prospects in the treatment of wastewater containing organic dye.

Experimental

Materials

Iron (III) chloride hexahydrate, polyethylene glycol (PEG-4000), anhydrous sodium acetate, ethylene glycol (EG), graphite powder, potassium permanganate, hydrogen peroxide, tetraethyl orthosilicate, cetyl trimethyl ammonium bromide (CTAB), bismuth nitrate pentahydrate, iron nitrate nonahydrate, potassium hydroxide, MO, Rh B, MB, ascorbic acid (VC), ethylene diamine tetraacetic acid (EDTA), isopropanol (IPA), benzyl quinone (BQ), and naphthol solution (5%) were obtained from commercial sources (Materials, Supplementary Material). All reagents were of analytical grade and used directly without any further purification. Distilled water was used in the experiments.

Preparation of the $Fe_3O_4@SiO_2@Bi_2O_2CO_3/rGO$ composite

Magnetic $Fe_3O_4@SiO_2$ microspheres were prepared following the method described in the literature (Liu et al. 2020). The $Fe_3O_4@SiO_2@Bi_2O_2CO_3/rGO$ was fabricated by means of a simple hydrothermal method. Specifically, 4.55 g of CTAB was dissolved in 100 mL of 50 wt% EG solution and ultrasonically stirred for 30 min to obtain a CTAB-EG solution. Afterward, a mixed solution obtained by dissolving 2.45 g of $Bi(NO_3)_3 \cdot 5H_2O$ and 2.05 g of $Fe(NO_3)_3 \cdot 9H_2O$ in 100 mL distilled water was gradually added dropwise to the CTAB-EG solution, and the pH of the mixture was adjusted to 10.5 by a dropwise addition of 10 mol/L KOH solution. After the mixture was stirred for 4 h at 25 °C, 1.00 g of the as-prepared $Fe_3O_4@SiO_2$ was added to the solution and ultrasonicated for 30 min to obtain a new mixture. Meanwhile, a graphene oxide (GO) suspension was prepared by ultrasonically dispersing different amounts of GO prepared via the improved Hummers method (Ribao et al. 2017) in 100 mL distilled water for 15 min. After the mixture and the GO suspension were mixed and stirred for 15 min, VC (three times the mass of GO) was added to the mixture, and the mixture was stirred for 30 min. The reaction mixture was transferred to a Teflon™-lined stainless steel autoclave with a 100 mL capacity. The autoclave was sealed and heated at 200 °C and maintained for 4 h. Subsequently, the autoclave was naturally cooled to room temperature, and the black particles were separated from the reaction mixture by an external magnet. The extracted particles were washed thoroughly with distilled water and anhydrous alcohol. The washing and magnetic separation cycle was repeated thrice. The final product, designated as $Fe_3O_4@SiO_2@Bi_2O_2CO_3/rGO$ (x) (where x refers to the mass of GO in the initial mixture, g), was acquired by drying the collected black particles at 80 °C for 24 h. Meanwhile, $Fe_3O_4@SiO_2@Bi_2O_2CO_3$ was prepared by following the

same procedure and conditions except for the addition of GO and VC.

Characterization

X-ray diffraction (XRD) analysis, Fourier transform infrared spectroscopy (FTIR), Raman spectrum, scanning electron microscopy (SEM), transmission electron microscopy (TEM), Brunauer–Emmett–Teller (BET) surface analysis, and vibrating sample magnetometry (VSM) were employed to characterize the structures and properties of the as-prepared samples. X-ray photoelectric spectroscopy (XPS) was used to investigate the surface composition and chemical state of $Fe_3O_4@SiO_2@Bi_2O_2CO_3/rGO$. UV–Vis DRS was conducted to investigate the optical absorption property of the photocatalyst. PL was used to investigate the separation and recombination of photogenic carriers. EIS test was used to determine the compound rate of carriers and the transfer capacity of surface charge in $Fe_3O_4@SiO_2@Bi_2O_2CO_3/rGO$. TOC analysis was conducted to determine the mineralization degree of the photocatalytic degradation reaction (Analysis details, Supplementary Material).

Visible-light catalytic degradation activity evaluation

Photodegradation performance for individual dye solution

The visible-light catalytic activity of the as-prepared $Fe_3O_4@SiO_2@Bi_2O_2CO_3/rGO$ was evaluated by photodegrading the MO, Rh B, and MB solutions. The photodegradation tests were performed in a CEL–LB70 photochemical reactor (Beijing China Education Au-light Co., Ltd., China) by using a 300 W Xe lamp as the simulated solar light source and a 100-mL double-jacketed beaker equipped with a circulating cooling system as the reactor, 50 mg of $Fe_3O_4@SiO_2@Bi_2O_2CO_3/rGO$ was added to the reaction solution (50 mL of 20 mg/L MO, Rh B, and MB solution) and stirred for 1 h in the dark to reach an adsorption–desorption equilibrium. During photodegradation, 2 mL of the suspension was collected every 15 min and separated via an external magnetic field to be used later for further analysis. The residual concentrations of the organic dyes were determined by using a UV–Vis spectrophotometer (Shimadzu Corporation, Japan) at 465 nm (MO), 554 nm (Rh B), and 665 nm (MB). All photocatalytic experiments were performed in triplicate, and the average of the experiments was analyzed. The photodegradation kinetics of the as-prepared catalyst could be described by the Langmuir–Hinshelwood kinetics model (Eq. (1)) (Thompson et al. 2020).

$$\ln\frac{C_0}{C_t} = k_{app}t, \tag{1}$$

where k_{app} refers to the quasi-first-order degradation rate

constant, and C_0 and C_t (mg/L) respectively refer to the concentrations of MO, Rh B, or MB initially and at time t, respectively.

The TOC of the MO solution degraded by $Fe_3O_4@SiO_2@Bi_2O_2CO_3/rGO$ (x = 0.15 g) was measured every 15 min, and the TOC removal efficiency (R_{TOC}) was calculated by using the following formula.

$$R_{TOC}(\%) = \frac{TOC_0 - TOC_t}{TOC_0} \times 100, \qquad (2)$$

where TOC_0 and TOC_t represent the initial TOC of the test solution and that at time t, respectively.

Decolorization performance for the mixed dye solution

The mixed dye solution was prepared by dissolving MO, Rh B, and MB at 5 mg each in 1 L distilled water. Photodegradation experiments were conducted according to the method and procedures described in the "Photodegradation performance for individual dye solution" section. The samples were collected every 15 min, and the chroma of the degradation solution was determined by using the dilution multiple method after the $Fe_3O_4@SiO_2@Bi_2O_2CO_3/rGO$ (x = 0.15 g) was separated and collected by an external magnet.

Visible-light catalytic degradation mechanism studies

UV–Vis DRS, PL, and EIS test

The detailed procedures of the UV-vis DRS, PL spectroscopy, and EIS measurement are described in Photoelectrochemical measurement of the Supplemental Material.

Capture experiment

An active species-trapping experiment was conducted by using various scavengers, including BQ, EDTA, and IPA, to trap and ascertain the reactive species (superoxide radical •O_2^-, photo-induced hole h$^+$, and hydroxyl radical •OH) during photodegradation. The experiment was performed the same way as that described in the "Photodegradation performance for individual dye solution" section except for the addition of scavengers. The concentration of the scavengers in the reaction system was 1.0 mmol/L.

Results and discussion

Characterization of the materials

The XRD patterns of the as-prepared Fe_3O_4, $Fe_3O_4@SiO_2$, $Fe_3O_4@SiO_2@Bi_2O_2CO_3$, and $Fe_3O_4@SiO_2@Bi_2O_2CO_3/rGO$ are shown in Fig. 1.
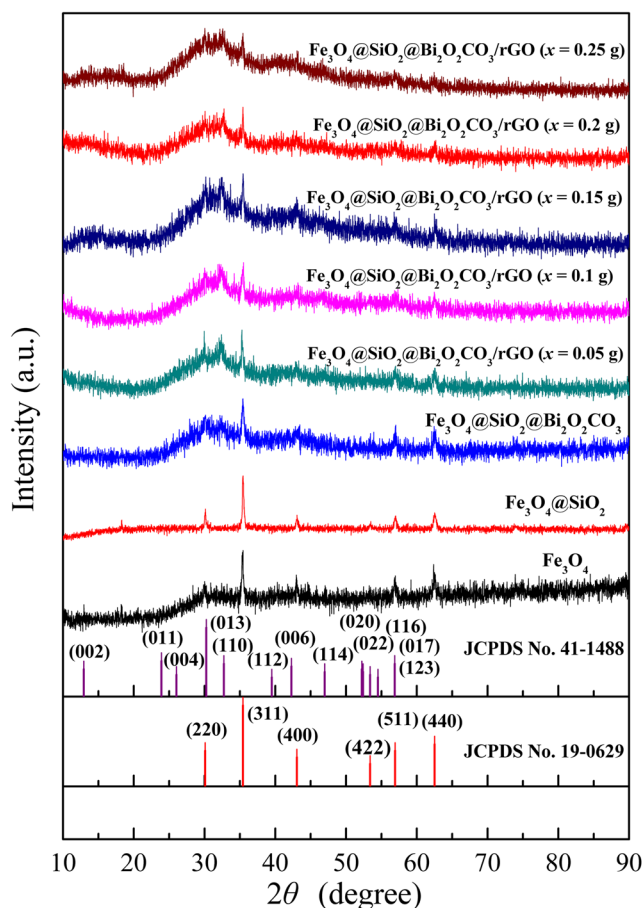

Fig. 1 XRD patterns of Fe_3O_4, $Fe_3O_4@SiO_2$, and $Fe_3O_4@SiO_2@Bi_2O_2CO_3/rGO$ (x)

The XRD patterns of Fe_3O_4 and $Fe_3O_4@SiO_2$ were consistent with the results reported in our previous work (Su et al. 2021). For $Fe_3O_4@SiO_2@Bi_2O_2CO_3$, apart from the corresponding peaks of Fe_3O_4, the new emerging diffraction peaks at 23.9°, 30.3°, 32.7°, and 48.9° were in line with those of the anatase structure of $Bi_2O_2CO_3$ (JCPDS No. 41-1488) (Kang et al. 2019), thereby suggesting that $Bi_2O_2CO_3$ formed and covered the $Fe_3O_4@SiO_2$. The main diffraction peaks assigned to $Fe_3O_4@SiO_2@Bi_2O_2CO_3$ appeared in the $Fe_3O_4@SiO_2@Bi_2O_2CO_3/rGO$ patterns except for some weakened diffraction peaks. However, a new broad peak appeared in the range of 20°–30° in each XRD pattern, which may be due to the low doping amount of rGO (Wang et al. 2017). These results indicate that the $Fe_3O_4@SiO_2@Bi_2O_2CO_3/rGO$ composite was successfully fabricated, and the composition process did not change the phase of the original $Fe_3O_4@SiO_2@Bi_2O_2CO_3$ microspheres. The weakened intensity of the peaks assigned to $Fe_3O_4@SiO_2@Bi_2O_2CO_3$ may be attributed to the noncrystalline rGO that reduced the proportion of the crystalline core in the composite material (Liu et al. 2019b). In addition, no significant characteristic diffraction peaks of GO can be seen in Fig. 1, thereby suggesting that GO was reduced completely. The diffraction intensity of each XRD pattern in the range of 20°–30°

did not change significantly along with an increasing amount of rGO, thereby suggesting that the amount of rGO had a negligible effect on the diffraction intensity of the as-prepared materials. Furthermore, the basic phases were the same for $Fe_3O_4@SiO_2@Bi_2O_2CO_3/rGO$ despite different amounts of rGO.

The FT-IR spectra of the as-prepared Fe_3O_4, $Fe_3O_4@SiO_2$, $Fe_3O_4@SiO_2@Bi_2O_2CO_3$, and $Fe_3O_4@SiO_2@Bi_2O_2CO_3/rGO$ are shown in Fig. 2A. The peaks at 588, 1645 and 3430 cm^{-1}, in the Fe_3O_4 curve (Fig. 2A[a]) and those at 466, 588, 786, 1051, 1082, and 1112 cm^{-1} (Fig. 2A[b]) were consistent with the results reported in our previous work (Liu et al. 2020; Su et al. 2021). These results suggest that the Fe_3O_4 and $Fe_3O_4@SiO_2$ microspheres were successfully prepared. As can be seen in Fig. 2A(c), new weak peaks appeared at 623, 839, and 1383 cm^{-1}, which can be ascribed to the stretching vibration of the Bi−O bond in $Bi_2O_2CO_3$ and the out-of-plane bending and antisymmetric vibration of CO_3^{2-} (Wang et al. 2018; Yang et al. 2019), whereas the peaks at 466, 1051, and 1082 cm^{-1} ascribed to $Fe_3O_4@SiO_2$ were weakened and even disappeared. As shown in Fig. 2A(d), the peaks at 623, 839, and 1383 cm^{-1} ascribed to $Bi_2O_2CO_3$ became stronger when $Bi_2O_2CO_3$ was formed in the presence of rGO in the as-prepared $Fe_3O_4@SiO_2@Bi_2O_2CO_3/rGO$. The peaks near 3430 cm^{-1} and 1645 cm^{-1} can be ascribed to the stretching and bending vibrations of −OH on the surface of the as-prepared samples, and the adsorbed water. Despite adding GO to the prepared of $Fe_3O_4@SiO_2@Bi_2O_2CO_3/rGO$, the peaks centered at 1050, 1270, and 1380 cm^{-1}, which can be ascribed to the stretching vibrations of C−O, C−O−C, and C−OH (He and Lu 2017), were not observed in the spectrum of $Fe_3O_4@SiO_2@Bi_2O_2CO_3/rGO$ ($x = 0.15$ g) in Fig. 2A(d). This finding indicates that GO was reduced to rGO in our reaction system and that the as-prepared composite

photocatalyst comprised $Fe_3O_4@SiO_2$, $Bi_2O_2CO_3$, and rGO components. The presence of rGO promoted and improved the structure formation of the photoactivity layer of $Bi_2O_2CO_3$ and increased the hydrophobicity of the as-prepared composite photocatalyst to a certain extent. Such a phenomenon can change the chemical environment, improve the surface properties of the composite photocatalyst, and benefit the improved interaction between the as-prepared $Fe_3O_4@SiO_2@Bi_2O_2CO_3/rGO$ and dye molecule with aromatic rings, thereby further enhancing the photocatalytic degradation towards the dye molecules. Therefore, $Fe_3O_4@SiO_2@Bi_2O_2CO_3/rGO$ was successfully fabricated.

Raman spectra were used to further investigate the structure of $Fe_3O_4@SiO_2@Bi_2O_2CO_3/rGO$. As shown in Fig. 2B, the intense peaks at 217 cm^{-1} and 276 cm^{-1} in the Raman spectrum of the Fe_3O_4 microspheres can be attributed to the A1g mode of the symmetric stretch of oxygen atoms along the Fe–O bonds (Sun et al. 2021). After coating the $Bi_2O_2CO_3$ layer and compositing with rGO, the corresponding peaks assigned to Fe_3O_4 were significantly weakened, which may be attributed to the coating of $Bi_2O_2CO_3$ and rGO on the surfaces of the Fe_3O_4 microspheres. $Bi_2O_2CO_3$ and rGO increased the size of the composite, thereby moving the inner Fe_3O_4 core away from the particle surface and consequently reducing the proportion of magnetic Fe_3O_4 in the $Fe_3O_4@SiO_2@Bi_2O_2CO_3/rGO$ composites. Meanwhile, new and weaker wide peaks appeared at regions near 1320 cm^{-1} and 1580 cm^{-1}. These peaks represent the ideal graphite structure and the defects and disordered carbon impurities on the graphite microcrystalline (Li et al. 2019), indicating that rGO was composited in $Fe_3O_4@SiO_2@Bi_2O_2CO_3$.

Figure 3 shows the morphologies of the as-prepared Fe_3O_4, $Fe_3O_4@SiO_2$, $Fe_3O_4@SiO_2@Bi_2O_2CO_3$, and $Fe_3O_4@SiO_2@Bi_2O_2CO_3/rGO$. Although the morphologies
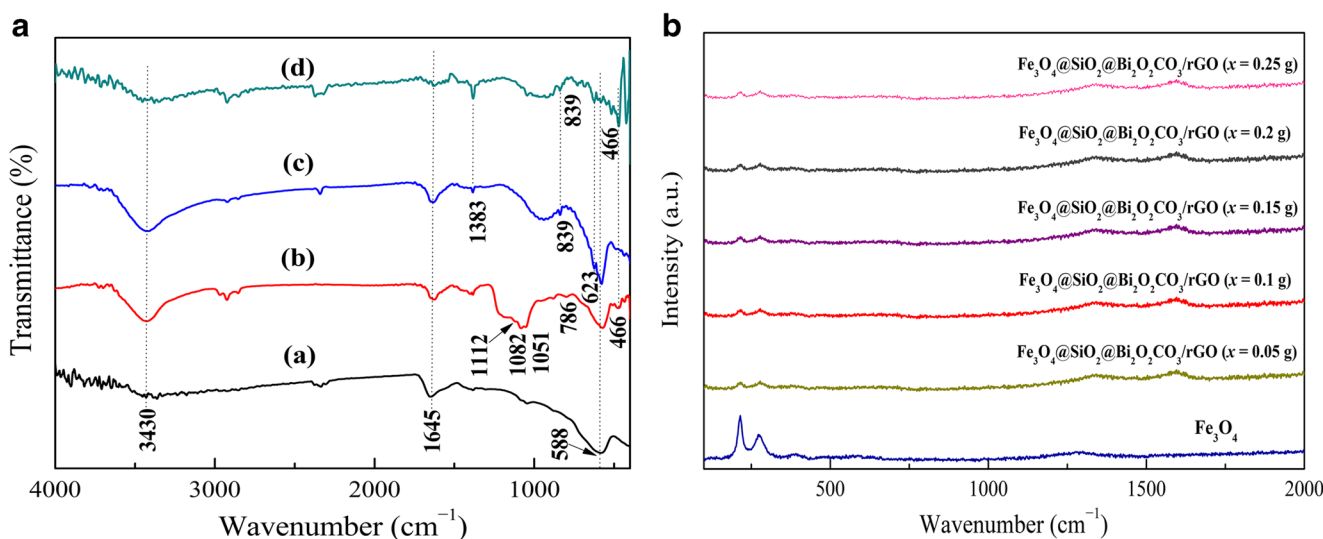
Fig. 2 A. FT-IR spectra of (**a**) Fe_3O_4, (**b**) $Fe_3O_4@SiO_2$, (**c**) $Fe_3O_4@SiO_2@Bi_2O_2CO_3$, and (**d**) $Fe_3O_4@SiO_2@Bi_2O_2CO_3/rGO$ ($x = 0.15$ g); B. Raman spectra of Fe_3O_4 and $Fe_3O_4@SiO_2@Bi_2O_2CO_3/rGO$ (x)

Fig. 3 SEM images of the as-prepared samples: (**a**) Fe$_3$O$_4$, (**b**) Fe$_3$O$_4$@SiO$_2$, (**c**) Fe$_3$O$_4$@SiO$_2$@Bi$_2$O$_2$CO$_3$, (**d**) Fe$_3$O$_4$@SiO$_2$@Bi$_2$O$_2$CO$_3$/rGO; TEM images of the as-prepared samples: (**e**) Fe$_3$O$_4$@SiO$_2$, (**f**) Fe$_3$O$_4$@SiO$_2$@Bi$_2$O$_2$CO$_3$/rGO (x = 0.15 g)
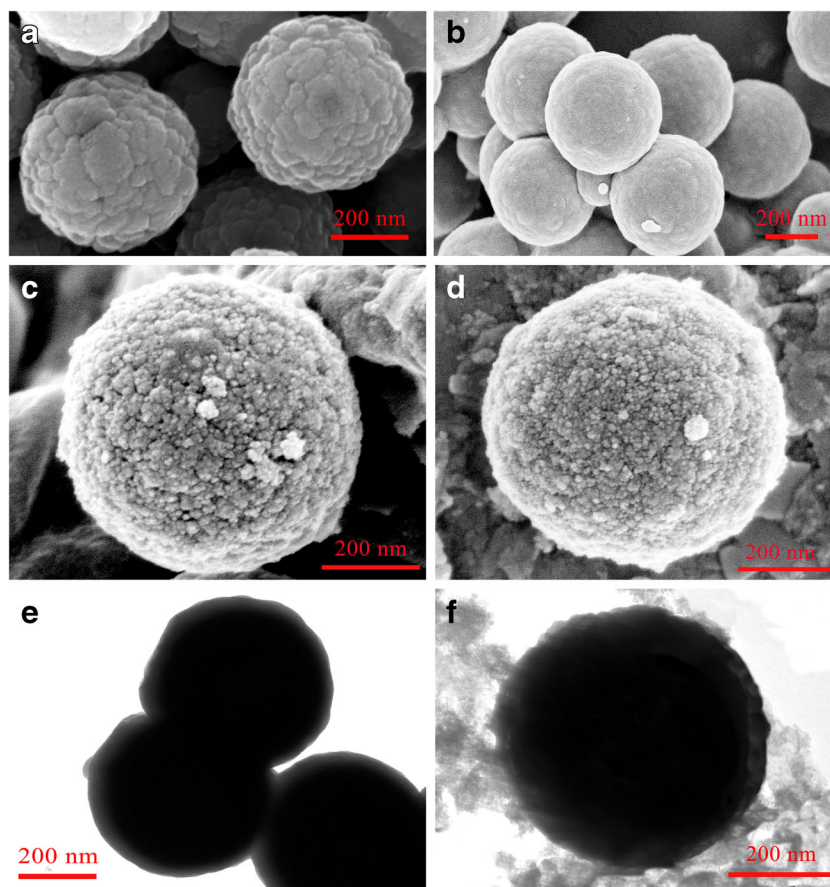
of the as-prepared Fe$_3$O$_4$ [Fig. 3(a)] and Fe$_3$O$_4$@SiO$_2$ [Fig. 3(b) and (e)] were discussed in our previous report (Liu et al. 2020; Su et al. 2021), they are still shown in Fig. 3 for a convenient comparison. The surface morphology of Fe$_3$O$_4$@SiO$_2$ [Fig. 3(b)] was similar to that of bared Fe$_3$O$_4$ [Fig. 3(a)] after coating the SiO$_2$ layer; however, the surface became smooth, and the particle size slightly increased from approximately 425 to 450 nm [Fig. 3(b) and (e)].

After further loading with Bi$_2$O$_2$CO$_3$, the Fe$_3$O$_4$@SiO$_2$@Bi$_2$O$_2$CO$_3$ microspheres exhibited spherical and uneven surface morphologies that were covered densely with many small globular particles with villi, and the average particle size increased to approximately 500 nm (Fig. 3[c]) with a narrow size distribution. In the fabrication of Fe$_3$O$_4$@SiO$_2$@Bi$_2$O$_2$CO$_3$/rGO in the presence of GO (Fig. 3[d]), the basic morphologies and particle size of Fe$_3$O$_4$@SiO$_2$@Bi$_2$O$_2$CO$_3$ loaded onto some flaky substances were unchanged, thereby suggesting that the GO and its transformation of GO to rGO had negligible effects on their basic structures. These phenomena may be attributed to the generated Bi$_2$O$_2$CO$_3$ that is preferentially loaded onto the surface of Fe$_3$O$_4$@SiO$_2$ to form uniform core–shell structural Fe$_3$O$_4$@SiO$_2$@Bi$_2$O$_2$CO$_3$ owing to the high similarity between Fe$_3$O$_4$@SiO$_2$ and Bi$_2$O$_2$CO$_3$ in terms of their surface properties. Given the significant natural differences between

Bi$_2$O$_2$CO$_3$ and rGO, the generated Bi$_2$O$_2$CO$_3$ cannot be easily grown on rGO as carriers or dependents. However, given that Fe$_3$O$_4$@SiO$_2$@Bi$_2$O$_2$CO$_3$ was formed in the presence of rGO or GO, the formed Fe$_3$O$_4$@SiO$_2$@Bi$_2$O$_2$CO$_3$ and rGO complement or fused their structures, and the as-prepared Fe$_3$O$_4$@SiO$_2$@Bi$_2$O$_2$CO$_3$/rGO formed a stable composite structure. The TEM images of Fe$_3$O$_4$@SiO$_2$ and Fe$_3$O$_4$@SiO$_2$@Bi$_2$O$_2$CO$_3$/rGO are shown in Fig. 3(e)–(f). The Fe$_3$O$_4$@SiO$_2$ microspheres had a uniform core–shell structure with a solid black core of approximately 425 nm and a gray layer of approximately 25 nm as shown in Fig. 3(e). This finding suggests that the SiO$_2$ layer was evenly and tightly coated on the surface of the Fe$_3$O$_4$ microspheres. The as-obtained Fe$_3$O$_4$@SiO$_2$@Bi$_2$O$_2$CO$_3$/rGO shown in Fig. 3(f) comprised microspheres cladded with a granular coating of approximately 50 nm dispersed on the black rGO nanosheets. The distinctive granular porous structure of the Bi$_2$O$_2$CO$_3$ coating layer on the Fe$_3$O$_4$@SiO$_2$ microspheres benefited light absorption and can improve the photocatalytic degradation performance of organic matters. The as-prepared Fe$_3$O$_4$@SiO$_2$@Bi$_2$O$_2$CO$_3$/rGO was fabricated by the uniform core–shell Fe$_3$O$_4$@SiO$_2$@Bi$_2$O$_2$CO$_3$ mounted on the rGO sheet.

The N$_2$ adsorption–desorption isotherms and the pore size distribution curves of the as-prepared Fe$_3$O$_4$@SiO$_2$@Bi$_2$O$_2$CO$_3$

and $Fe_3O_4@SiO_2@Bi_2O_2CO_3/rGO$ ($x = 0.15$ g) are presented in Fig. 4(a), and the corresponding parameters are shown in Table S1. The abovementioned materials possessed an IV-type gas adsorption isotherm with an H4-type hysteresis loop. The specific surface areas, pore volumes, and pore diameters of $Fe_3O_4@SiO_2@Bi_2O_2CO_3$ and $Fe_3O_4@SiO_2@Bi_2O_2CO_3/rGO$ ($x = 0.15$ g) were 83.84 m^2/g and 102.12 m^2/g, 0.19 m^3/g and 0.29 m^3/g, and 9.13 nm and 11.21 nm, respectively. These values indicate that the two materials were naturally mesoporous (Cheng et al. 2020). Large specific surface areas and porous structures can provide more active sites for the photocatalytic reaction, increase the utilization of visible light, and eventually improve the photocatalytic performance.

The magnetization saturation curves of the bared Fe_3O_4 particles, $Fe_3O_4@SiO_2$, $Fe_3O_4@SiO_2@Bi_2O_2CO_3$, and $Fe_3O_4@SiO_2@Bi_2O_2CO_3/rGO$ ($x = 0.15$ g) are shown in Fig. 4(b). The specific parameters of the saturation magnetization of $Fe_3O_4@SiO_2@Bi_2O_2CO_3/rGO$ (x) (magnetization saturation [M_s], negligible magnetic remnant [M_r], and coercivity [H_c]) are shown in Table S2. The M_s values of the as-prepared materials decreased along with the increase in composite components, and the M_s of $Fe_3O_4@SiO_2@Bi_2O_2CO_3/rGO$ ($x = 0.15$ g) was 61.9 emu/g lower than that of the bared Fe_3O_4 particles. However, the as-prepared $Fe_3O_4@SiO_2@Bi_2O_2CO_3/rGO$ ($x = 0.05$–0.25 g) continuously exhibited an excellent magnetic response for effective magnetic separation. This finding may be ascribed to the decreased proportion of magnetic Fe_3O_4 core in the $Fe_3O_4@SiO_2@Bi_2O_2CO_3/rGO$ composite due to the deposition of non-magnetic components onto the surface of the composites. In addition, the M_r and H_c values of the as-prepared $Fe_3O_4@SiO_2@Bi_2O_2CO_3/rGO$ ($x = 0.05$–0.25 g) indicate that these samples had superparamagnetic behaviors. As shown in the lower right corner of Fig. 4(b), the as-prepared samples can be enriched within 10 s by applying an external permanent magnet and redispersed after withdrawing the magnet, indicating that such samples have outstanding magnetic separation performance and redispersibility, and are good for recycling.

Figure 5 shows the surface composition and chemical state of $Fe_3O_4@SiO_2@Bi_2O_2CO_3/rGO$ based on the results of an XPS analysis. Bi (158.32 eV), C (284.36 eV), Si (101.07 eV), Fe (709.7 eV), and O (529.13 eV) were presented in the full-range curve of $Fe_3O_4@SiO_2@Bi_2O_2CO_3/rGO$ as shown in Fig. 5(a), thereby suggesting that the as-prepared $Fe_3O_4@SiO_2@Bi_2O_2CO_3/rGO$ comprised Bi, C, Si, Fe, and O. Fig. 5(b) shows the O 1s spectrum of the $Fe_3O_4@SiO_2@Bi_2O_2CO_3/rGO$ comprising three peaks with differentiated binding energies of 531.5, 531.2, and 528.9 eV, which can be ascribed to the oxygen peaks of the hydroxyl carboxyl groups in the $Bi_2O_2CO_3$ lattice, oxygen in rGO, and interfacial Si–O–Bi cross-linking bonds, respectively. Figure 5(c) shows the Bi 4f spectrum of $Fe_3O_4@SiO_2@Bi_2O_2CO_3/rGO$ comprising two peaks with differentiated binding energies of 163.7 eV and 158.4 eV, which can be ascribed to Bi $4f_{5/2}$ and Bi $4f_{7/2}$ of Bi^{3+}, respectively. The positions of the two peaks significantly shifted relative to those of $Bi_2O_2CO_3$, indicating that rGO and $Bi_2O_2CO_3$ had a certain interface effect in the hydrothermal process (Huang et al. 2016). As shown in Fig. 5(d), the C 1s spectrum of $Fe_3O_4@SiO_2@Bi_2O_2CO_3/rGO$ was divided into the following four characteristic peaks: the peak at 284.2 eV assigned to the C−C bond in rGO. the peak at 284.7 eV assigned to the C−O bond in the epoxy and hydroxyl groups, the peak at 285.8 eV assigned to the C=O bond in the carboxyl group (Gong et al. 2019), and the peak at 287.3 eV assigned to the carbonate ion in $Bi_2O_2CO_3$. Thereafter, the C 1s of the GO spectrum was fitted to the three characteristic peaks. The
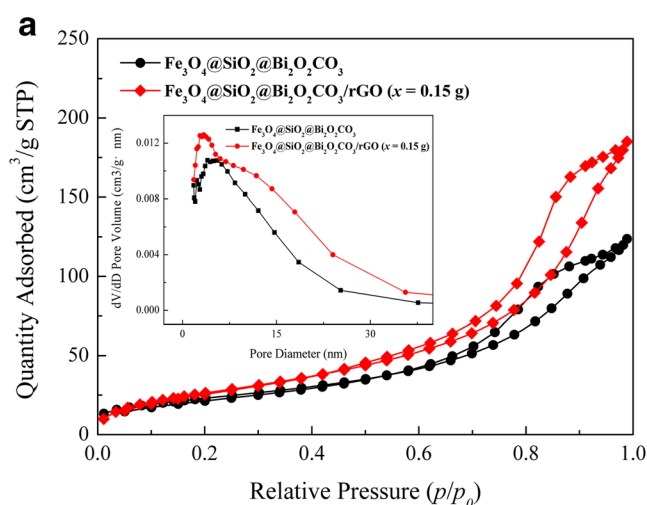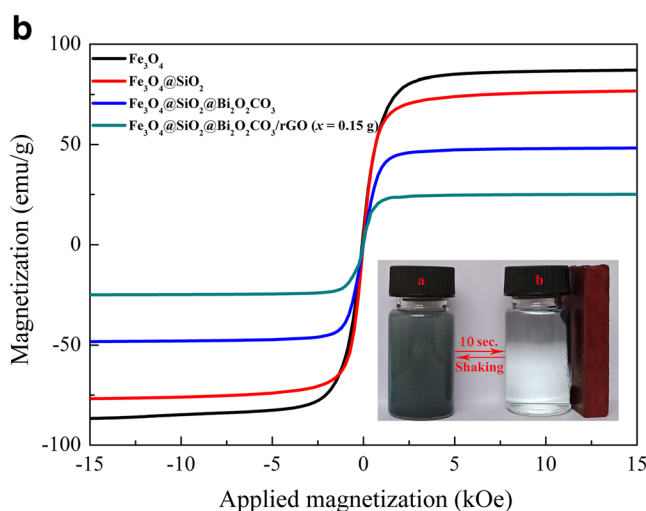

Fig. 4 (a) N_2 adsorption–desorption isotherms of $Fe_3O_4@SiO_2@Bi_2O_2CO_3$ and $Fe_3O_4@SiO_2@Bi_2O_2CO_3/rGO$ ($x = 0.15$ g); (b) magnetic hysteresis loops of $Fe_3O_4@SiO_2@Bi_2O_2CO_3/rGO$ microsphere (Insets: the photograph of magnetic separation and redispersion)
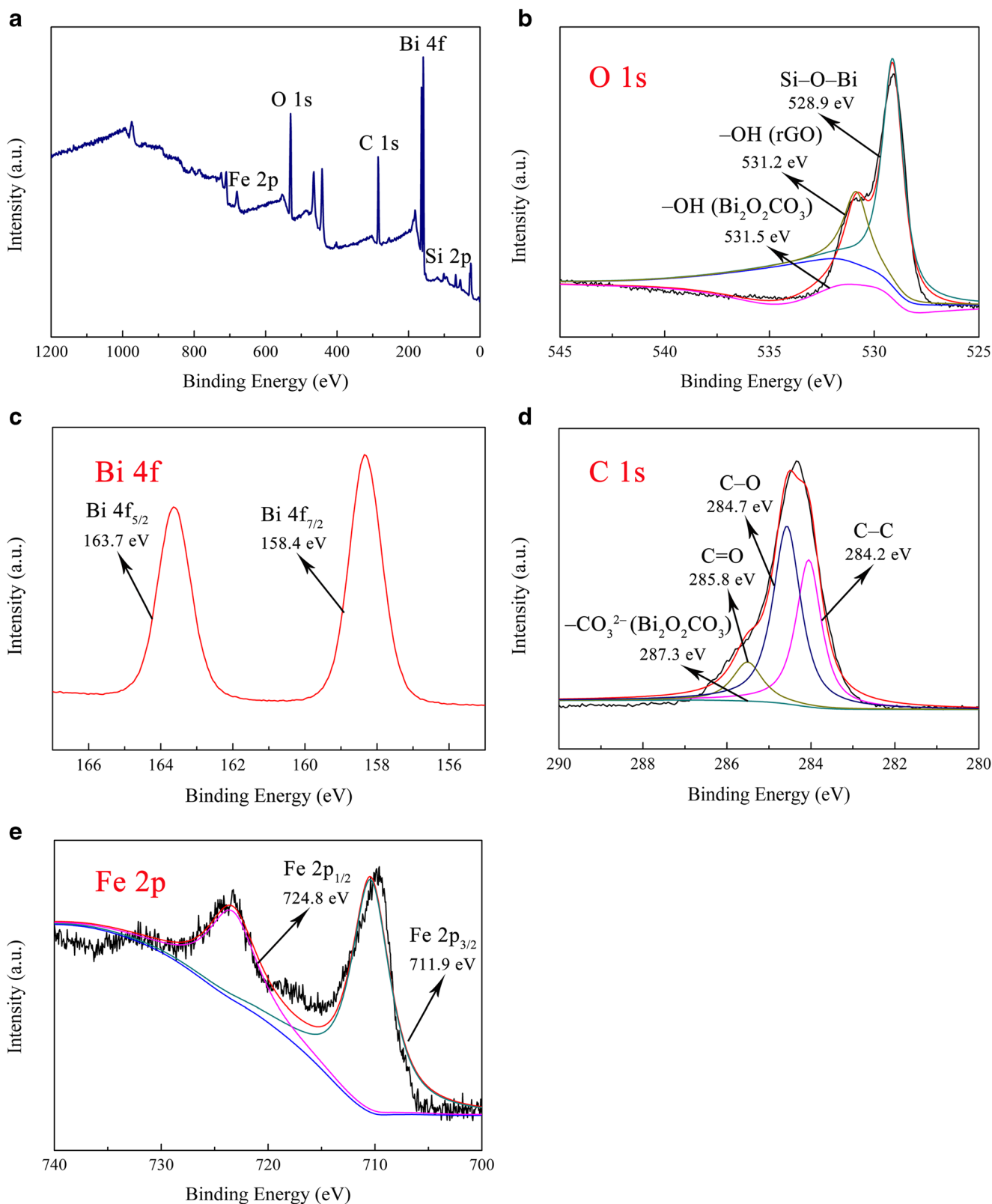
Fig. 5 XPS spectra (**a**) full range, (**b**) O 1s, (**c**) Bi 4f, (**d**) C 1s, and (**e**) Fe 2p of $Fe_3O_4@SiO_2@ Bi_2O_2CO_3/rGO$ ($x = 0.15$ g)

peaks at 284.9, 286.6, and 287.5 eV corresponded to the binding energies of C−C, C−O, and C=O bonds, respectively (Li et al. 2016a). The peak strengths of C−C and C=O in $Fe_3O_4@SiO_2@Bi_2O_2CO_3/rGO$ were lower than those of

GO, indicating that GO was reduced. As shown in Fig. 5(e), the Fe 2p spectrum of $Fe_3O_4@SiO_2@Bi_2O_2CO_3/rGO$ comprised two peaks with differentiated binding energies of 711.9 eV and 724.8 eV that can be assigned to Fe $2p_{3/2}$ and Fe $2p_{1/2}$, thereby confirming the presence of Fe_3O_4.

Photocatalytic activity

Photocatalytic degradation performance for a single dye solution

Figure 6 shows the photocatalytic degradation performance of $Fe_3O_4@SiO_2@Bi_2O_2CO_3/rGO$ for the MO, Rh B, and MB single-organic dye solutions under visible-light irradiation.

As shown in Fig. 6(a), the degradation rates of MO, Rh B, and MB by the as-prepared $Fe_3O_4@SiO_2@Bi_2O_2CO_3/rGO$ (x = 0.15 g) in the dark were low and generally unchanged after 15 min. The corresponding degradation rates were 10.4%, 8.3%, and 6.4%. The degradation rates of these dyes can be ascribed to adsorption. Results also indicate that adsorption/desorption equilibrations can be achieved within 15 min and that the affinity of the dye molecule to the photocatalyst follows the order of MO > Rh B > MB. Their corresponding photodegradation rates significantly increased and reached 99.3%, 61.6%, and 39.1% at the photocatalyst dosage of 1 g/L after 90 min of irradiation. The photodegradation rates of the three dyes significantly differed from one another, with $Fe_3O_4@SiO_2@Bi_2O_2CO_3/rGO$ (x = 0.15 g) exhibiting the highest photocatalytic activity to MO degradation. The photodegradation rate for MO was considerably higher than those of the other photocatalysts reported in the literature as shown in Table 1. Such discrepancy may be ascribed to the different molecular structures of the dyes (Table 2) (Ahmad et al. 2020; Rabbani et al. 2017) and their adsorption behaviors as depicted on the surface of the photocatalyst. On the one hand, the photocatalytic activity was greatly influenced by the adsorption behaviors of the photocatalyst toward the dye molecules because the photocatalytic reaction occurs on the surface of the photocatalyst. The adsorption behaviors were largely dependent on the structure of the photocatalyst and the size and properties of the dye molecules. Given that $Fe_3O_4@SiO_2@Bi_2O_2CO_3/rGO$ (x = 0.15 g) was naturally mesoporous (11.21 nm, Table S1), the dye molecule with a smaller size and surface properties similar to those of the photocatalyst was more likely to penetrate the pore to generate stronger adsorption. The $Fe_3O_4@SiO_2@Bi_2O_2CO_3/rGO$ (x = 0.15 g) exhibited the same photodegradation rates sequence as the adsorption (or affinity) order (MO > Rh B > MB). On the other hand, the dye molecules played a direct and important role in the photocatalysis. In the photodegradation of the three dyes, given the same photocatalyst and light irradiation conditions, the species and amount of the photogenerated active species ($\bullet O_2^-$, $\bullet OH$, and h^+) were the same in the degradation of dyes, resulting in the oxidation contribution of the active

species to the degradation should be equal. However, the three dyes remarkably differed in terms of their molecular structures. MO is an anionic azo dye, Rh B is a cationic xanthene compound dye with four N-ethyl groups attached to both sides of the xanthene rings, and MB is a blue cationic thiazine dye (Jabeen et al. 2020). Two different reaction pathways, namely, the oxidation caused by $\bullet O_2^-$, $\bullet OH$, and h^+ and the reduction arising from the electron transfer from the conduction band to the azo bond, may be involved in the degradation of azo dyes in a photocatalytic system (Tang and Huren 1995) except that MO molecules were oxidatively degraded by the photogenerated active species and that the azo bond in MO molecules can be reduced by the electron transfer from the conduction band of the photocatalyst. This phenomenon can rupture the conjugation system and degrade the MO molecules (Tang and Huren 1995). Therefore, the reduction caused by the electrons in the conduction band may explain why MO had a higher degradation rate than the other two dyes. The higher photodegradation rate of Rh B than MB by the photocatalyst can also be ascribed to the better affinity of the photocatalyst towards Rh B, thereby making it easier to be captured by the active site on the photocatalyst (Borthakur et al. 2016).

Figure 6(b) shows the effects of the as-prepared photocatalysts with different amounts of rGO on the photodegradation rate of MO. The degradation rate increased along with irradiation time, and the photodegradation rates by the $Fe_3O_4@SiO_2@Bi_2O_2CO_3/rGO$ composites were significantly higher than those by the $Fe_3O_4@SiO_2@Bi_2O_2CO_3$. The photodegradation rate of MO by the $Fe_3O_4@SiO_2@Bi_2O_2CO_3/rGO$ with 0.15 g of rGO was the highest. When the irradiation time was 90 min, the photodegradation rate of MO by $Fe_3O_4@SiO_2@Bi_2O_2CO_3$ was only 55.6%, whereas those by the composited $Fe_3O_4@SiO_2@Bi_2O_2CO_3/rGO$ all exceeded 60% and that by $Fe_3O_4@SiO_2@Bi_2O_2CO_3/rGO$ (x = 0.15 g) was nearly 100%. This finding indicates that the photocatalytic activity of the as-prepared materials can be significantly improved by composing a suitable amount of rGO. This finding may be attributed to the improvement in the structure and surface property of the as-prepared photocatalyst and the interaction between the photocatalyst and MO molecules. Figure 6(c) shows the relationship between $ln\frac{C_0}{C_t}$ and the reaction time (t) of $Fe_3O_4@SiO_2@Bi_2O_2CO_3@rGO$. The good linear relationships between $ln\frac{C_0}{C_t}$ and t indicate that the photodegradation of MO by $Fe_3O_4@SiO_2@Bi_2O_2CO_3/rGO$ conformed to the first-order kinetic reaction. The k_{app} of $Fe_3O_4@SiO_2@Bi_2O_2CO_3/rGO$ (x = 0.15 g) was 0.05553 min^{-1}, which was 6.81 times larger than that of $Fe_3O_4@SiO_2@Bi_2O_2CO_3$ (0.00816 min^{-1}) and higher than those of the other $Fe_3O_4@SiO_2@Bi_2O_2CO_3/rGO$ (x). The optimal composite amount of rGO in $Fe_3O_4@SiO_2@Bi_2O_2CO_3/rGO$ was 0.15 g. Figure 6(d) shows the absorption spectra of
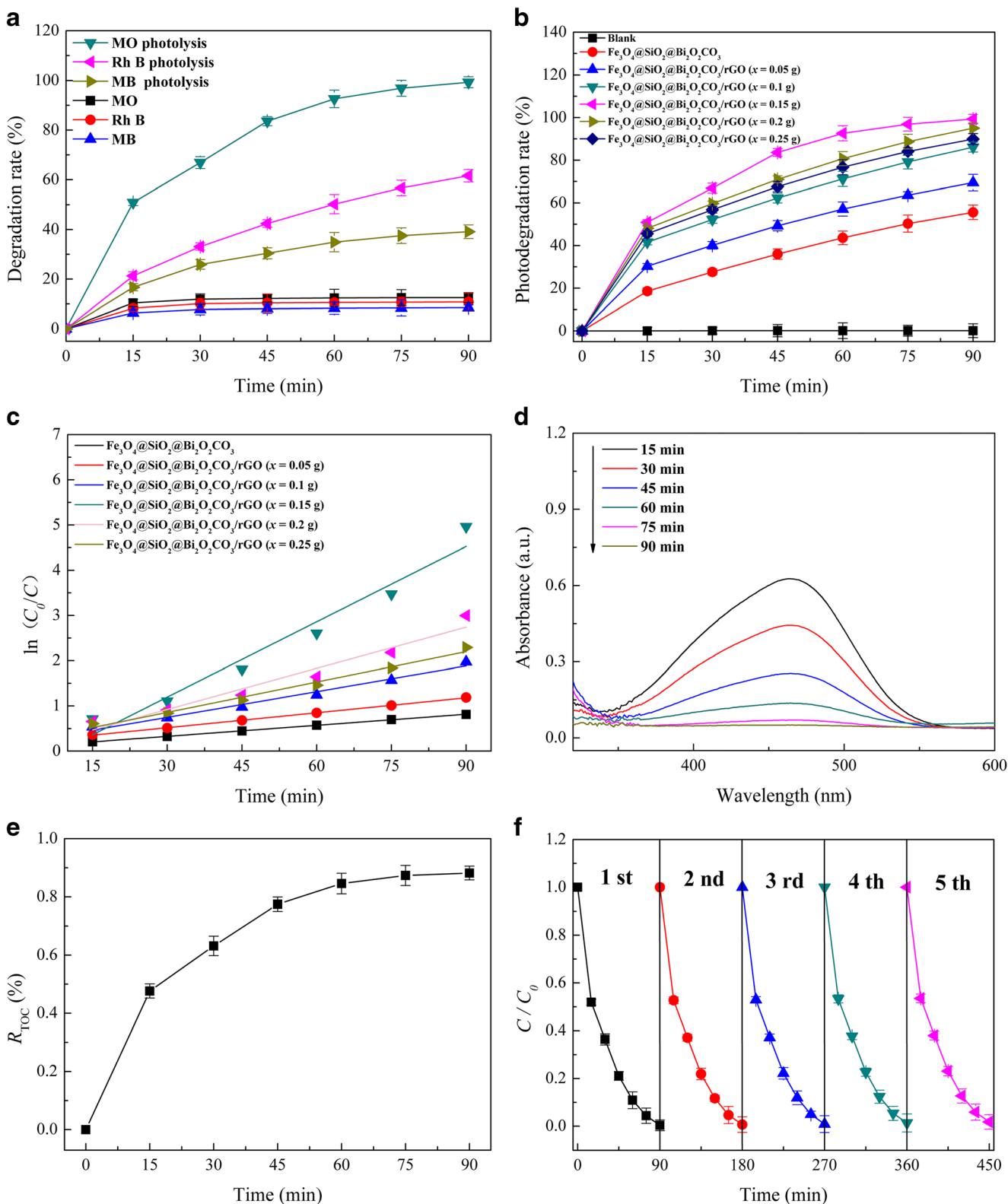
Fig. 6 (**a**) Degradation rates of MO, Rh B, and MB in the absence and presence of $Fe_3O_4@SiO_2@Bi_2O_2CO_3$/rGO ($x = 0.15$ g); (**b**) photodegradation rates of MO by $Fe_3O_4@SiO_2@Bi_2O_2CO_3$/rGO ($x$) with different amounts of rGO; (**c**) kinetic linear fitting curves of the photodegradation of MO by $Fe_3O_4@SiO_2@Bi_2O_2CO_3$/rGO ($x$) with different amounts of rGO; (**d**) UV–visible absorption spectra of $Fe_3O_4@SiO_2@Bi_2O_2CO_3$/rGO ($x = 0.15$ g); (**e**) change in the TOC removal efficiency (R_{TOC}) with irradiation time ; (**f**) recyclability of the $Fe_3O_4@SiO_2@Bi_2O_2CO_3$/rGO ($x = 0.15$ g) in the photodegradation of MO solution via external magnetic separation
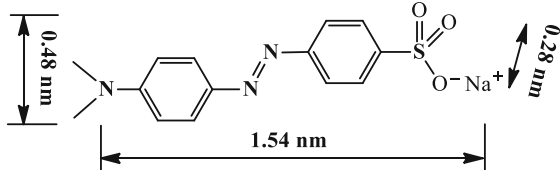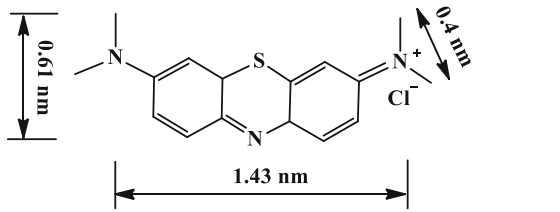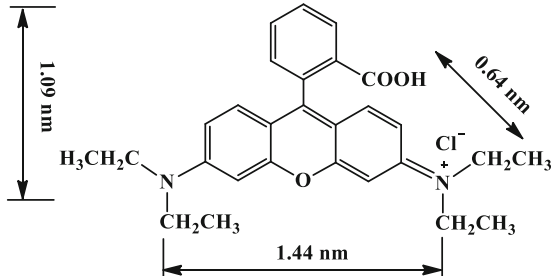
Table 1 Comparison of photocatalytic degradation performance of $Fe_3O_4@SiO_2@Bi_2O_2CO_3/rGO$ ($x = 0.15$ g) toward MO with other reported photocatalysts

Photocatalyst	Catalyst dosage (g/L)	MO concentration (mg/L)	Light source	Time (min)	Degradation rate (%)	References
$Graphene/Bi_2O_2CO_3$	0.3	20	UV	12	39	(Ao et al. 2015)
$Graphene/Bi_2O_2CO_3/TiO_2$	0.3	20	UV	12	94	(Ao et al. 2015)
$Ag_2CrO_4-Bi_2O_2CO_3$	1.0	10	Vis	120	82	(Fan et al. 2019)
$Co_3O_4-C_3N_4$	1.0	10	Vis	180	99	(Han et al. 2014)
$Ag_2CO_3/Bi_2O_2CO_3$	1.0	10	Vis	40	96	(Li et al. 2016a)
Cu_3SnS_4/TiO_2	1.0	10	Vis	120	82	(Li et al. 2017)
Ag/TiO_2	1.0	10	UV	60	92	(Ling et al. 2019)
FTO/BiOBr	4.0	10	Vis	300	48	(Liu et al. 2014)
TiO_2	0.6	3.5	UV-vis	50	41	(Peng et al. 2013)
$Ag/Bi_2O_2CO_3$	0.6	3.5	UV-vis	50	91	(Peng et al. 2013)
$g-C_3N_4/Ag_2WO_4$	1.0	10	Vis	150	95	(Zhu et al. 2017)
$Fe_3O_4@SiO_2@Bi_2O_2CO_3$	1.0	20	Vis	90	55.6	This work
$Fe_3O_4@SiO_2@Bi_2O_2CO_3/rGO$ ($x = 0.15$ g)	1.0	20	Vis	90	99.3	This work

MO under the catalysis of $Fe_3O_4@SiO_2@Bi_2O_2CO_3/rGO$ ($x = 0.15$ g). The absorption strength of MO degraded by $Fe_3O_4@SiO_2@Bi_2O_2CO_3/rGO$ ($x = 0.15$ g) in the UV–

Visible region completely disappeared after 90 min of photocatalysis. Furthermore, the maximum absorption peak of MO did not show a blue shift, thereby suggesting that the

Table 2 Molecular structure and absorbance maximum (λ_{max}) of the organic dyes

Dye	Molecular structure	MW	λ_{max} (nm)
MO		327.3	465
MB		319.9	665
Rh B		479.4	554

photodegradation was primarily caused by photocatalytic chromophore cracking (Memon et al. 2018). This finding is consistent with the abovementioned discussion, that is, the MO molecule was partially degraded by the reduction of the azo band associated with the photogenerated e^- in the conduction band of the photocatalyst. As shown in Fig. 6(e), the TOC removal efficiency by Fe_3O_4@SiO_2@$Bi_2O_2CO_3$/rGO (x = 0.15 g) for MO reached 88.2%, indicating that the as-prepared photocatalyst can effectively mineralize rather than simply decolor the MO molecules. Figure 6(f) shows the recycling catalytic degradation performance of Fe_3O_4@SiO_2@$Bi_2O_2CO_3$/rGO (x = 0.15 g) toward MO in five catalytic cycles. Fe_3O_4@SiO_2@$Bi_2O_2CO_3$/rGO (x = 0.15 g) was easily collected by the external magnet, washed successively with distilled water and ethanol, and reused in the succeeding photocatalytic cycle. The photodegradation of MO by the regenerated Fe_3O_4@SiO_2@$Bi_2O_2CO_3$/rGO (x = 0.15 g) slightly decreased, thereby indicating that the as-prepared Fe_3O_4@SiO_2@$Bi_2O_2CO_3$/rGO (x = 0.15 g) had excellent reusability and stability.

Decolorization for the mixed organic dyes solution

The photodegradation capabilities of Fe_3O_4@SiO_2@$Bi_2O_2CO_3$/rGO (x = 0.15 g) toward the mixed dye solution in five catalytic cycles are shown in Fig. S1. In the five cycles, the solution tended to be colorless after being irradiated for 75 min and became completely discolored at 90 min in the first and second cycles (Figs. S1 1st and 2nd). In the first two cycles, the as-prepared Fe_3O_4@SiO_2@$Bi_2O_2CO_3$/rGO (x = 0.15 g) exhibited a certain reduction in decolorization for the mixed dye solution. In the last three cycles, the decolorization ability of Fe_3O_4@SiO_2@$Bi_2O_2CO_3$/rGO (x = 0.15 g) was generally unchanged. Therefore, after five cycles, Fe_3O_4@SiO_2@$Bi_2O_2CO_3$/rGO (x = 0.15 g) maintained a high decolorization effect for the mixed organic dyes solution, thereby highlighting its excellent photocatalytic degradation ability and recyclability. This result indicates that the as-prepared Fe_3O_4@SiO_2@$Bi_2O_2CO_3$/rGO has broad prospects in treating industrial wastewater containing organic dyes.

Visible-light photocatalytic mechanism

The UV–vis DRS of Fe_3O_4@SiO_2@$Bi_2O_2CO_3$/rGO (x = 0, 0.05, 0.1, 0.15, 0.2, and 0.25 g) is shown in Fig. 7(a). The absorbance values of Fe_3O_4@SiO_2@$Bi_2O_2CO_3$/rGO composited with different amounts of rGO were all higher than that of Fe_3O_4@SiO_2@$Bi_2O_2CO_3$, particularly those of Fe_3O_4@SiO_2@$Bi_2O_2CO_3$/rGO with rGO amounts of 0.15 g and 0.20 g. This finding indicates that a suitable amount of rGO can broaden the response of the catalyst to visible light

and significantly improve the utilization of visible light. The $Bi_2O_2CO_3$ layer was the active substance that absorbed light; the n value of $Bi_2O_2CO_3$ was 4 because it functioned as an indirect semiconductor (Ding et al. 2019). The band gap (E_g) values of Fe_3O_4@SiO_2@$Bi_2O_2CO_3$/rGO with rGO amounts of 0, 0.05, 0.1, 0.15, 0.2, and 0.25 g were 3.27, 3.21, 3.16, 3.05, 3.13, and 3.19 eV, respectively, according to Eq. (S1) (Photoelectrochemical measurement, Supplementary Material). These values were lower than those of $Bi_2O_2CO_3$ (3.3 eV–3.5 eV) (Fan et al. 2019). The E_g of Fe_3O_4@SiO_2@$Bi_2O_2CO_3$/rGO with an rGO amount of 0.15 g was the lowest (3.05 eV), which corresponds to the highest photodegradation rate (Fig. 6[b]). Therefore, the $Bi_2O_2CO_3$ layer in the as-prepared photocatalysts was hierarchically nanostructured and composed of fluffy particles, that can produce multiple reflected and scattered light, thereby increasing the probability of light absorption (SSR effect) (Wang et al. 2021). In addition, a suitable amount of rGO can effectively promote e^-/h^+ separation (Benavente et al. 2019).

Figure 7(b) shows the PL spectra of the Fe_3O_4@SiO_2@$Bi_2O_2CO_3$/rGO composites with an Xe lamp excitation wavelength of 370 nm. The strongest peak corresponds to the energy released by the excitation of the electron transition back to the valence band from the conduction band, resulting in a photo-induced e^-/h^+ recombination. The PL intensity values of all Fe_3O_4@SiO_2@$Bi_2O_2CO_3$/rGO samples were significantly lower than that of Fe_3O_4@SiO_2@$Bi_2O_2CO_3$ and reached the minimum for Fe_3O_4@SiO_2@$Bi_2O_2CO_3$/rGO (x = 0.15 g). These results indicate that photocarrier recombination was effectively inhibited by the composition with a suitable amount of rGO. The amount of rGO was 0.15 g, which can effectively suppress the photo-induced e^-/h^+ recombination rate. Therefore, the optimal amount of GO should be 0.15 g.

EIS was used to analyze the interfacial transfer capabilities of Fe_3O_4@SiO_2@$Bi_2O_2CO_3$ and Fe_3O_4@SiO_2@$Bi_2O_2CO_3$/rGO (x = 0.15 g; Fig. 7[c]). The arc radius of the Nyquist curve for Fe_3O_4@SiO_2@$Bi_2O_2CO_3$/rGO (x = 0.15 g) was significantly smaller than that of Fe_3O_4@SiO_2@$Bi_2O_2CO_3$ under simulated solar irradiation, implying that the photo-induced charge of Fe_3O_4@SiO_2@$Bi_2O_2CO_3$/rGO (x = 0.15 g) at the interface migration resistance decreased, whereas the charge mobility was enhanced (Zhang et al. 2019b). This result accords with those of the PL test, thereby confirming the highest photodegradation rate at the rGO amount of 0.15 g.

Figure 7(d) shows the effects of scavengers on the degradation of MO by Fe_3O_4@SiO_2@$Bi_2O_2CO_3$/rGO (x = 0.15 g). The MO solution was completely decolorized after 90 min of photocatalytic degradation in the absence of any scavenger. However, the degradation for MO was inhibited in varying degrees after adding the trapping agents of EDTA, IPA, and BQ. The photocatalytic degradation rate of MO was only 40.3% after adding BQ, 50.9% for IPA, and 60.6% for EDTA after 90 min of
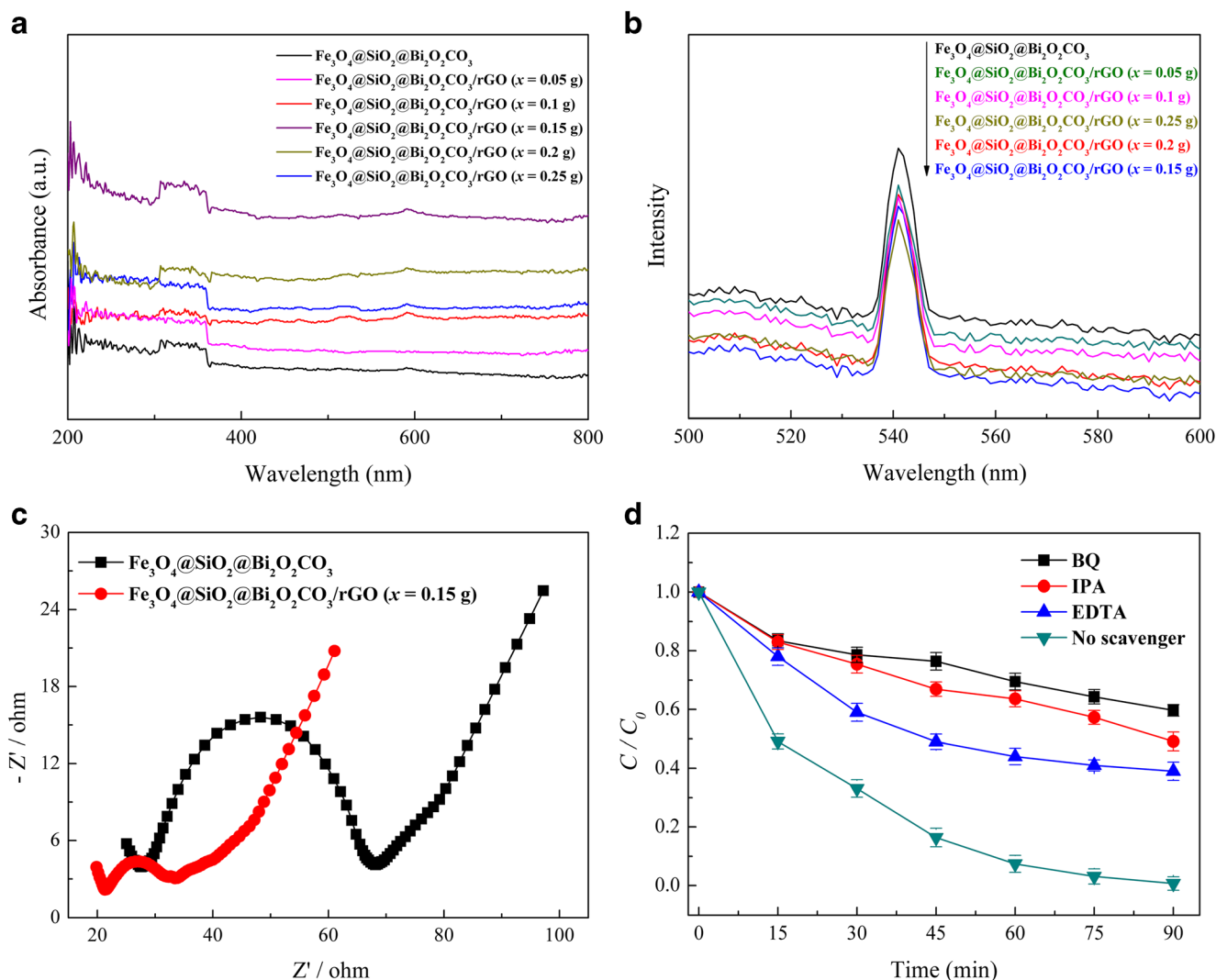
Fig. 7 (**a**) UV–vis diffuse reflectance spectra, (**b**) PL spectra, and (**c**) EIS Nyquist curves of $Fe_3O_4@SiO_2@Bi_2O_2CO_3$ and $Fe_3O_4@SiO_2@Bi_2O_2CO_3/rGO$ (x); (**d**) the effects of scavengers on the photodegradation of MO by $Fe_3O_4@SiO_2@Bi_2O_2CO_3/rGO$ ($x = 0.15$ g)

degradation. Consequently, the inhibition degree followed the order of BQ > IPA > EDTA. These results indicate that $\cdot O_2^-$ was the primary oxidative specie, followed by $\cdot OH$ and h^+, which contributed to the degradation of MO. Therefore, the visible-light catalytic degradation of MO by $Fe_3O_4@SiO_2@Bi_2O_2CO_3/rGO$ ($x = 0.15$ g) was the result of the attack and decomposition of various active species ($\cdot O_2^-$, $\cdot OH$, and h^+), among which $\cdot O_2^-$ was the dominant active species.

The mechanism of photogenic carrier separation and migration on the $Fe_3O_4@SiO_2@Bi_2O_2CO_3/rGO$ interface can be summarized based the abovementioned analysis as follows. The $Fe_3O_4@SiO_2@Bi_2O_2CO_3/rGO$ were excited to produce h^+ and e^- under visible light exposure. The rGO can rapidly transfer photo-induced e^- to its surface through the large conjugated π bond structure, thereby effectively blocking the recombination of photo-induced h^+ and e^-. Given that the conduction band potential of $Bi_2O_2CO_3$

(−0.76 eV) (Zhao et al. 2015) was lower than the standard electrode potential of $O_2/\cdot O_2^-$ (−0.33 eV; vs. NHE) (He et al. 2019), the photo-induced e^- on the surfaces of $Fe_3O_4@SiO_2@Bi_2O_2CO_3$ and rGO can be captured by O_2 molecules on their surface to produce $\cdot O_2^-$. Moreover, some photo-induced e^- can be transferred directly from the conduction band to the azo band, thereby allowing the dye molecules with azo band (MO) to undergo reductive degradation. As for the photo-induced h^+, the valence band potential of 2.29 eV was higher than the standard electrode potential of $H_2O/\cdot OH$ at 1.99 eV (vs. NHE) (Huang et al. 2015). Therefore, H_2O or OH^- in the solution can be oxidized to $\cdot OH$. Meanwhile, h^+ can directly oxidize organic dye molecules adsorbed on its surface. The organic dye molecules were degraded and mineralized under the synergistic oxidation of $\cdot O_2^-$, $\cdot OH$, and h^+. MO can also be degraded by the photo-induced e^- reduction in the conduction band of $Fe_3O_4@SiO_2@Bi_2O_2CO_3/rGO$.

Conclusions

A novel magnetic $Fe_3O_4@SiO_2@Bi_2O_2CO_3$/rGO composite was successfully fabricated by using $Fe_3O_4@SiO_2$ microspheres as a magnetic core through a simple hydrothermal method. The as-prepared $Fe_3O_4@SiO_2@Bi_2O_2CO_3$/rGO composites comprised uniform core–shell-structured $Fe_3O_4@SiO_2@Bi_2O_2CO_3$ microspheres that were mounted on rGO sheets. The unique structure, high surface area, and mesoporous channels endowed the as-prepared photocatalyst with high light harvest and abundant active reaction sites. $Fe_3O_4@SiO_2@Bi_2O_2CO_3$/rGO ($x = 0.15$ g) possessed excellent photocatalytic degradation activity for MO and decolorization performance for the mixed solution of MO, Rh B, and MB. The photodegradation rate and TOC removal efficiency of MO by $Fe_3O_4@SiO_2@Bi_2O_2CO_3$/rGO ($x = 0.15$ g) were 99.3% and 88.2%, respectively. The photodegradation of MO by $Fe_3O_4@SiO_2@Bi_2O_2CO_3$/rGO ($x = 0.15$ g) conformed to the first-order kinetic reaction, and the corresponding k_{app} was 0.05553 min^{-1}, which was 6.81 times larger than that of $Fe_3O_4@SiO_2@Bi_2O_2CO_3$ and higher than those of the other $Fe_3O_4@SiO_2@Bi_2O_2CO_3$/rGO ($x$). A suitable amount of rGO in the as-prepared photocatalyst can ~~decrease~~ reduce the energy band gap and accelerate the transfer of photo-induced electrons and provide multiple sites for the O_2-capturing photoinduced electrons to form active species $•O_2^-$, thereby inhibiting the recombination of light e^-/h^+ pairs, and broadening and enhancing the response of the catalyst to visible light, and improving the visible-light catalytic degradation for the organic dyes. The active species produced in the photocatalysis included $•O_2^-$, $•OH$, and h^+, with $•O_2^-$ being the dominant active species. Moreover, the as-prepared photocatalysts had excellent magnetic separation performance that benefited continuous and automatic operation, recyclability, and stability. The results demonstrate that the as-prepared $Fe_3O_4@SiO_2@Bi_2O_2CO_3$/rGO composite is a photocatalyst with high application potential in organic dye removal.

Author contribution Lihua Liu initiated and designed the research. Gang Su contributed to the experiment, writing, and development of the manuscript. Lixing Zhang, Xing Liu, Jianrong Xue, and Anping Tang aided in analyzing the results. All authors discussed the results and contributed to the final manuscript. All authors are informed and agree to the study.

Declarations

Ethics approval Not applicable.

Consent for publication All the co-authors agreed to publish the manuscript.

Competing interests The authors declare no competing interests.

References

Ahmad M, Aziz ARA, Mazari SA, Baloch AG, Nizamuddin S (2020) Photocatalytic degradation of methyl orange from wastewater using a newly developed Fe-Cu-Zn-ZSM-5 catalyst. Environ Sci Pollut Res 27:26239–26248. https://doi.org/10.1007/s11356-020-08940-9

Anwer H, Mahmood A, Lee J, Kim K-H, Park J-W, Yip ACK (2019) Photocatalysts for degradation of dyes in industrial effluents: Opportunities and challenges. Nano Res 12:955–972. https://doi.org/10.1007/s12274-019-2287-0

Ao Y, Xu L, Wang P, Wang C, Hou J, Qian J, Li Y (2015) Graphene and TiO_2 co-modified flower-like $Bi_2O_2CO_3$: A novel multi-heterojunction photocatalyst with enhanced photocatalytic activity. Appl Surf Sci 355:411–418. https://doi.org/10.1016/j.apsusc.2015.07.027

Benavente E, Aliaga J-A, Barraza P, Araya J-F, Farías M-H, González G, Alonso-Núñez G (2019) Melamine-assisted synthesis of nitrogen-doped ReS_2 nanosheets/carbon composites. Mater Lett 243:42–45. https://doi.org/10.1016/j.matlet.2019.01.152

Bian Y, Ma Y, Shang Y, Tan P, Pan J (2018) Self-integrated beta-Bi_2O_3/$Bi_2O_{2.33}@Bi_2O_2CO_3$ ternary composites: Formation mechanism and visible light photocatalytic activity. Appl Surf Sci 430:613–624. https://doi.org/10.1016/j.apsusc.2017.06.063

Borthakur P, Boruah PK, Darabdhara G, Sengupta P, Das MR, Boronin AI, Kibis LS, Kozlova MN, Fedorov VE (2016) Microwave assisted synthesis of CuS-reduced graphene oxide nanocomposite with efficient photocatalytic activity towards azo dye degradation. J Environ Chem Eng 4:4600–4611. https://doi.org/10.1016/j.jece.2016.10.023

Cheng Z, Saad A, Guo H, Wang C, Liu S, Thomas T, Yang M (2020) Ordered mesoporous transition metal nitrides prepared through hard template nanocasting and rapid nitridation process. J Alloys Compd 838:155375. https://doi.org/10.1016/j.jallcom.2020.155375

Deng P, Wang H, Qi R, Zhu J, Chen S, Yang F, Zhou L, Qi K, Liu H, Xia BY (2020) Bismuth Oxides with Enhanced Bismuth–Oxygen Structure for Efficient Electrochemical Reduction of Carbon Dioxide to Formate. ACS Catal 10:743–750. https://doi.org/10.1021/acscatal.9b04043

Ding P, Di J, Chen X, Zhao J, Gu K, Zhang Y, Yin S, Liu G, Xia J, Li H (2019) Partially etched $Bi_2O_2CO_3$ by metal chloride for enhanced reactive oxygen species generation: A tale of two strategies. Appl Catal B-Environ 245:325–333. https://doi.org/10.1016/j.apcatb.2018.12.047

Do Q-C, Kim D-G, Ko S-O (2018) Catalytic activity enhancement of a $Fe_3O_4@SiO_2$ yolk-shell structure for oxidative degradation of

acetaminophen by decoration with copper. J Clean Prod 172:1243–1253. https://doi.org/10.1016/j.jclepro.2017.10.246

Fan H, Zhou H, Li H, Liu X, Ren C, Wang F, Li W (2019) Novel $Ag_2CrO_4/Bi_2O_2CO_3$ heterojunction: Simple preparation, wide visible-light absorption band and excellent photocatalytic activity. Chem Phys 517:60–66. https://doi.org/10.1016/j.chemphys.2018.09.031

Gong J, Hao Y, Li L, Xue S, Xie P, Hou X, Feng H, Wei X, Liu Z, Xu Z, Huang J (2019) The preparation and photocatalytic performance research of CdSe and wool ball-like GO/CdSe microspheres. J Alloys Compd 779:962–970. https://doi.org/10.1016/j.jallcom.2018.11.278

Guo S, Min Y, Fan J, Xu Q (2016) Holey Structured Graphitic Carbon Nitride Thin Sheets with Edge Oxygen doping via photo-Fenton reaction with Enhanced Photocatalytic Activity. Appl Catal B-Environ 185:315–321. https://doi.org/10.1016/j.apcatb.2015.11.030

Gurusamy L, Anandan S, Wu JJ (2017) Synthesis of Reduced Graphene Oxide Supported Flower-like Bismuth Subcarbonates Microsphere ($Bi_2O_2CO_3$-RGO) for Supercapacitor Application. Electrochim Acta 244:209–221. https://doi.org/10.1016/j.electacta.2017.05.098

Han C, Ge L, Chen C, Li Y, Xiao X, Zhang Y, Guo L (2014) Novel visible light induced Co_3O_4-g-C_3N_4 heterojunction photocatalysts for efficient degradation of methyl orange. Appl Catal B-Environ 147:546–553. https://doi.org/10.1016/j.apcatb.2013.09.038

He HY, Lu J (2017) Highly photocatalytic activities of magnetically separable reduced graphene oxide-$CoFe_2O_4$ hybrid nanostructures in dye photodegradation. Sep Purif Technol 172:374–381. https://doi.org/10.1016/j.seppur.2016.08.040

He B, Liu H, Lin Z, Yan L, Ning J, Zhong Y, Zheng C, Zhang Z, Hu Y (2019) A new photocatalyst based on $Co(CO_3)_{0.5}(OH)\cdot0.11H_2O$/$Bi_2WO_6$ nanocomposites for high-efficiency cocatalyst-free O_2 evolution. Chem Eng J 359:924–932. https://doi.org/10.1016/j.cej.2018.11.094

Huang H, He Y, Du X, Chu PK, Zhang Y (2015) A General and Facile Approach to Heterostructured Core/Shell $BiVO_4$/BiOI p–n Junction: Room-Temperature in Situ Assembly and Highly Boosted Visible-Light Photocatalysis. ACS Sustain Chem Eng 3:3262–3273. https://doi.org/10.1021/acssuschemeng.5b01038

Huang H, Ke X, Na T, Xin D, Zhang Y (2016) Dual visible-light active components containing self-doped $Bi_2O_2CO_3$/g-C_3N_4 2D-2D heterojunction with enhanced visible-light-driven photocatalytic activity. Colloid Surface A 511:64–72. https://doi.org/10.1016/j.colsurfa.2016.09.063

Jabeen S, Iqbal J, Arshad A, Awan MS, Warsi MF (2020) $(In_{1-x}Fe_x)_2O_3$ nanostructures for photocatalytic degradation of various dyes. Mater Chem Phys 243:122516. https://doi.org/10.1016/j.matchemphys.2019.122516

Jiang Y, Liu B, Xu J, Pan K, Yang J (2017) Cross-linked chitosan/β-cyclodextrin composite for selective removal of methyl orange: Adsorption performance and mechanism. Carbohydr Polym 182:106–114. https://doi.org/10.1016/j.carbpol.2017.10.097

Jiang G, Li X, Che Y, Lv Y, Liu F, Wang Y, Zhao C, Wang X (2019) Antibacterial and anticorrosive properties of CuZnO@RGO waterborne polyurethane coating in circulating cooling water. Environ Sci Pollut Res 26:9027–9040. https://doi.org/10.1007/s11356-019-04374-0

Kang W, Lin B, Jiang Z, Liu Z, Feng L, Sun Y, Zhang X, Yang H, Huang G, Xing B, Zhang C (2019) $Bi_2O_2CO_3$ microspheres anchored on reduced graphene oxide nanosheets as electrode material for lithium ion batteries and supercapacitors. Mater Lett 240:299–302. https://doi.org/10.1016/j.matlet.2019.01.027

Li T, Hu X, Liu C, Tang C, Wang X, Luo S (2016a) Efficient photocatalytic degradation of organic dyes and reaction mechanism with $Ag_2CO_3/Bi_2O_2CO_3$ photocatalyst under visible light irradiation. J Mol Catal A-Chem 425:124–135. https://doi.org/10.1016/j.molcata.2016.10.001

Li Z-D, Wang H-L, Wei X-N, Liu X-Y, Yang Y-F, Jiang W-F (2016b) Preparation and photocatalytic performance of magnetic Fe_3O_4@TiO_2 core–shell microspheres supported by silica aerogels from industrial fly ash. J Alloys Compd 659:240–247. https://doi.org/10.1016/j.jallcom.2015.10.297

Li Y, Liu F-T, Chang Y, Wang J, Wang C-W (2017) High efficient photocatalytic activity from nanostructuralized photonic crystal-like p-n coaxial hetero-junction film photocatalyst of Cu_3SnS_4/TiO_2 nanotube arrays. Appl Surf Sci 426:770–780. https://doi.org/10.1016/j.apsusc.2017.07.258

Li J, Liu Y, Zhou Y, Liu S, Liang Y, Luo T, Dai G (2018) Enhanced visible-light photocatalytic activity of $Bi_2O_2CO_3$ nanoplates by Fe-doping in the degradation of rhodamine B. Mater Res Bull 107:438–445. https://doi.org/10.1016/j.materresbull.2018.08.018

Li K, Rimmer SM, Liu Q, Zhang Y (2019) Micro-Raman Spectroscopy of Microscopically Distinguishable Components of Naturally Graphitized Coals from Central Hunan Province, China. Energy Fuel 33:1037–1048

Li D, Yu P, Zhou X, Kim J-H, Zhang Y, Alvarez PJJ (2020) Hierarchical $Bi_2O_2CO_3$ wrapped with modified graphene oxide for adsorption-enhanced photocatalytic inactivation of antibiotic resistant bacteria and resistance genes. Water Res 184:116157. https://doi.org/10.1016/j.watres.2020.116157

Ling L, Feng Y, Li H, Chen Y, Wen J, Zhu J, Bian Z (2019) Microwave induced surface enhanced pollutant adsorption and photocatalytic degradation on Ag/TiO_2. Appl Surf Sci 483:772–778. https://doi.org/10.1016/j.apsusc.2019.04.039

Liu Z, Wu B, Niu J, Huang X, Zhu Y (2014) Solvothermal synthesis of BiOBr thin film and its photocatalytic performance. Appl Surf Sci 288:369–372. https://doi.org/10.1016/j.apsusc.2013.10.034

Liu J, Liang T, Tu R, Lai W, Liu Y (2019a) Redistribution of π and σ electrons in boron-doped graphene from DFT investigation. Appl Surf Sci 481:344–352. https://doi.org/10.1016/j.apsusc.2019.03.109

Liu L, Liu J, Zhao L, Yang Z, Lv C, Xue J, Tang A (2019b) Synthesis and characterization of magnetic Fe_3O_4@$CaSiO_3$ composites and evaluation of their adsorption characteristics for heavy metal ions. Environ Sci Pollut Res 26:8721–8736. https://doi.org/10.1007/s11356-019-04352-6

Liu L, Zhao L, Liu J, Yang Z, Su G, Song H, Xue J, Tang A (2020) Preparation of magnetic Fe_3O_4@SiO_2@$CaSiO_3$ composite for removal of Ag^+ from aqueous solution. J Mol Liq 299:112222. https://doi.org/10.1016/j.molliq.2019.112222

Marcelino RBP, Amorim CC (2019) Towards visible-light photocatalysis for environmental applications: band-gap engineering versus photons absorption—a review. Environ Sci Pollut Res 26:4155–4170. https://doi.org/10.1007/s11356-018-3117-5

Memon AA, Arbab AA, Patil SA, Mengal N, Sun KC, Sahito IA, Jeong SH, Kim HS (2018) Synthesis of solution processed f-CNT@Bi_2S_3 hybrid film coated linen fabric as a free-standing textile structured photo catalyst. Appl Catal A-Gen 566:87–95. https://doi.org/10.1016/j.apcata.2018.06.015

Minitha C-R, Lalitha M, Jeyachandran Y-L, Senthilkumar L, Rajendra Kumar R-T (2017) Adsorption behaviour of reduced graphene oxide towards cationic and anionic dyes: Co-action of electrostatic and π–π interactions. Mater Chem Phys 194:243–252. https://doi.org/10.1016/j.matchemphys.2017.03.048

Omrani N, Nezamzadeh-Ejhieh A (2020) $BiVO_4$/WO_3 nano-composite: characterization and designing the experiments in photodegradation of sulfasalazine. Environ Sci Pollut Res 27:44292–44305. https://doi.org/10.1007/s11356-020-10278-1

Peng S, Li L, Tan H, Wu Y, Cai R, Yu H, Huang X, Zhu P, Ramakrishna S, Srinivasan M, Yan Q (2013) Monodispersed Ag nanoparticles loaded on the PVP-assisted synthetic $Bi_2O_2CO_3$ microspheres with enhanced photocatalytic and supercapacitive performances. J Mater Chem A 1:7630–7638. https://doi.org/10.1039/c3ta10951h

Rabbani M, Seghatoleslami ZS, Rahimi R (2017) Selective adsorption of organic dye methylene blue by $Cs_4H_2PMo_{11}FeO_{40}\cdot 6H_2O$ in presence of methyl orange and Rhodamine-B. J Mol Struct 1146:113–118. https://doi.org/10.1016/j.molstruc.2017.05.134

Ran H, Lu J, Wang Z, Wang C, Li J, Zhang C, Wang X, He X, Hu C (2020) Two-dimensional $Bi_2O_2CO_3/\delta$-Bi_2O_3/Ag_2O heterojunction for high performance of photocatalytic activity. Appl Surf Sci 525:146613. https://doi.org/10.1016/j.apsusc.2020.146613

Ribao P, Rivero MJ, Ortiz I (2017) TiO_2 structures doped with noble metals and/or graphene oxide to improve the photocatalytic degradation of dichloroacetic acid. Environ Sci Pollut Res 24:12628–12637. https://doi.org/10.1007/s11356-016-7714-x

Su X, Wu D (2018) Controllable synthesis of plate BiOBr loaded plate $Bi_2O_2CO_3$ with exposed {001} facets for ciprofloxacin photo-degradation. J Ind Eng Chem 64:256–265. https://doi.org/10.1016/j.jiec.2018.03.023

Su G, Liu L, Liu X, Zhang L, Xue J, Tang A (2021) Magnetic $Fe_3O_4@SiO_2@BiFeO_3/rGO$ composite for the enhanced visible-light catalytic degradation activity of organic pollutants. Ceram Int 47:5374–5387. https://doi.org/10.1016/j.ceramint.2020.10.118

Sun Y-H, Huang M-X, Guan D-C, Zhang G-L, Wei J-L, Nan J-M, Yi F-Y (2021) Influence of the Sn(Fe)–C bonds content in $SnFe_2O_4@reduced$ graphene oxide composites on the electrochemical behavior of lithium-ion batteries. J Alloys Compd 854:157297. https://doi.org/10.1016/j.jallcom.2020.157297

Tang WZ, Huren A (1995) UV/TiO_2 photocatalytic oxidation of commercial dyes in aqueous solutions. Chemosphere 31:4157–4170. https://doi.org/10.1016/0045-6535(95)80015-D

Teixeira S, Mora H, Blasse L-M, Martins PM, Carabineiro SAC, Lanceros-Méndez S, Kühn K, Cuniberti G (2017) Photocatalytic degradation of recalcitrant micropollutants by reusable $Fe_3O_4/SiO_2/TiO_2$ particles. J Photochem Photobiol A-Chem 345:27–35. https://doi.org/10.1016/j.jphotochem.2017.05.024

Thompson WA, Sanchez Fernandez E, Maroto-Valer MM (2020) Probability Langmuir-Hinshelwood based CO_2 photoreduction kinetic models. Chem Eng J 384:123356. https://doi.org/10.1016/j.cej.2019.123356

Varma R, Chaurasia S, Patel N, Bhanage BM (2020) Interplay of adsorption, photo-absorption, electronic structure and charge carrier dynamics on visible light driven photocatalytic activity of Bi_2MoO_6/rGO (0D/2D) heterojunction. J Environ Chem Eng 8:104551. https://doi.org/10.1016/j.jece.2020.104551

Wang D, Yang J, Li X, Zhai H, Lang J, Song H (2016) Preparation of magnetic $Fe_3O_4@SiO_2@mTiO_2$–Au spheres with well-designed microstructure and superior photocatalytic activity. J Mater Sci 51:9602–9612. https://doi.org/10.1007/s10853-016-0167-2

Wang Q, Xing L, Xue X (2017) SnO_2-graphene nanocomposite paper as both the anode and current collector of lithium ion battery with high performance and flexibility. Mater Lett 209:155–158. https://doi.org/10.1016/j.matlet.2017.07.132

Wang A, Zhang J, Zhao W, Zhu W, Zhong Q (2018) Porphyrin decorated $Bi_2O_2CO_3$ nanocomposites with efficient difunctional properties of photocatalysis and optical nonlinearity. J Alloys Compd 748:929–937. https://doi.org/10.1016/j.jallcom.2018.03.217

Wang M-X, Zhu H, Yang G-J, Liu K, Li J-F, Kong L-T (2021) Solid-solution strengthening effects in binary Ni-based alloys evaluated by high-throughput calculations. Mater Des 198:109359. https://doi.org/10.1016/j.matdes.2020.109359

Wu X, Li H, Wang X, Jiang L, Xi J, Du G, Ji Z (2019) Ferroelectric enhanced photoelectrochemical water splitting in $BiFeO_3/TiO_2$ composite photoanode. J Alloys Compd 783:643–651. https://doi.org/10.1016/j.jallcom.2018.12.345

Yang B, Lv K, Li Q, Fan J, Li M (2019) Photosensitization of $Bi_2O_2CO_3$ nanoplates with amorphous Bi_2S_3 to improve the visible photoreactivity towards NO oxidation. Appl Surf Sci 495:143561. https://doi.org/10.1016/j.apsusc.2019.143561

Zang Y, Gong L, Mei L, Gu Z, Wang Q (2019) Bi_2WO_6 Semiconductor Nanoplates for Tumor Radiosensitization through High-Z Effects and Radiocatalysis. ACS Appl Mater Interfaces 11:18942–18952. https://doi.org/10.1021/acsami.9b03636

Zhang Y, Zhu G, Hojamberdiev M, Gao J, Hao J, Zhou J, Liu P (2016) Synergistic effect of oxygen vacancy and nitrogen doping on enhancing the photocatalytic activity of $Bi_2O_2CO_3$ nanosheets with exposed {001} facets for the degradation of organic pollutants. Appl Surf Sci 371:231–241. https://doi.org/10.1016/j.apsusc.2016.02.210

Zhang F, Peng H, Jiang S, Wang C, Xu X, Wang L (2019a) Construction of precious metal-loaded BiOI semiconductor materials with improved photocatalytic activity for microcystin-LR degradation. Environ Sci Pollut Res 26:8226–8236. https://doi.org/10.1007/s11356-019-04266-3

Zhang G-Y, Wang J-J, Shen X-Q, Wang J-J, Wang B-Y, Gao D-Z (2019b) Br-doped Bi2O2CO3 nanosheets with improved electronic structure and accelerated charge migration for outstanding photocatalytic behavior. Appl Surf Sci 470:63–73. https://doi.org/10.1016/j.apsusc.2018.11.103

Zhao Z, Zhou Y, Wang F, Zhang K, Yu S, Cao K (2015) Polyaniline-Decorated {001} Facets of $Bi_2O_2CO_3$ Nanosheets: In Situ Oxygen Vacancy Formation and Enhanced Visible Light Photocatalytic Activity. ACS Appl Mater Interfaces 7:730–737. https://doi.org/10.1021/am507089x

Zhao H, Li G, Tian F, Jia Q, Liu Y, Chen R (2019) g-C_3N_4 surface-decorated $Bi_2O_2CO_3$ for improved photocatalytic performance: Theoretical calculation and photodegradation of antibiotics in actual water matrix. Chem Eng J 366:468–479. https://doi.org/10.1016/j.cej.2019.02.088

Zhu B, Xia P, Li Y, Ho W, Yu J (2017) Fabrication and photocatalytic activity enhanced mechanism of direct Z-scheme g-C_3N_4/Ag_2WO_4 photocatalyst. Appl Surf Sci 391:175–183. https://doi.org/10.1016/j.apsusc.2016.07.104